Rare Metal Materials and Engineering
Volume
Available online at **www.rmme.ac.cn**

Cite this article as: Rare Metal Materials and Engineering,

DOI: 10.12442/j.issn.1002-185X.20240198

Preparation and High-Temperature Oxidation Performance Study of TiC-NiCr Cermet

Lei Zhang[1,2,4], Bensheng Huang[1,*], Chuandi Xie[2,4], Gen Chen[5], Jiao Du [2,4], Haishen Sun [2,3,4], Hanyang Zuo[6]

[1.] *School of New Energy and Materials, Southwest Petroleum University, Chengdu 610500, China*

[2.] *Shandong province key laboratory of powder metallurgy and advanced manufacture, Jinan271100, China*

[3.] *University of Science & Technology Beijing, Beijing 100083, China*

[4.] *Laiwu Vocational and Technical College, Metallurgical Department, Jinan 271100, China*

[5.] *EMI Pipeline Tech. Co., Ltd, Kunshan 215300, China*

[6.] *Material Corrosion and Protection Key Laboratory of Sichuan province,Zigong 643002, China*

Abstract: Cermets, known for their excellent hardness, strength, and wear resistance, have extensive applications in many industries. Currently, a significant research challenge involves enhancing the mechanical properties and oxidation resistance of metal-ceramics while reducing production costs through improvements in the ceramic phases and variations in the types and compositions of metals. In this study, we employed powder metallurgy to fabricate TiC-NiCr cermets and examined their oxidation behaviour at 900 ℃. The results revealed a uniformly structured TiC-NiCr cermets with excellent mechanical properties, exhibiting a Rockwell hardness value of (HRC65) and a flexural strength of 1450 MPa. This study investigates the high-temperature oxidation mechanism of TiC-based cermets using X-ray diffraction (XRD) and scanning electron microscopy (SEM) analysis. Incorporating Ni and Cr elements, along with their solid solutions, not only bonds the hard phase TiC to ensure the physical performance of the cermet but also impedes internal diffusion during oxidation by forming a dense composite oxide layer, thereby enhancing its oxidation resistance. The TiC-NiCr cermet exhibited a dense protective oxide film at 900 ℃ and endured continuous oxidation for approximately 1000 h. This paper presents a methodology for fabricating of TiC-NiCr metal matrix composites and evaluates their oxidation resistance, providing a theoretical and practical basis for enhancing both mechanical properties and oxidation resistance while reducing production costs.

Key words: TiC-NiCr; Microstructure; High Temperature Oxidation; Thermodynamics and Kinetics.

1 Introduction

Cermets are heterogeneous composite materials composed of a mixture of one or more ceramic phases with a metal, with the ceramic phase typically constituting 100–90% of the material volume. These composites exhibit a unique combination of metallic properties—including good toughness, electrical conductivity, and thermal conductivity and ceramic characteristics such as high strength, hardness, wear resistance, high-temperature stability, and excellent chemical stability. Consequently, they have emerged as crucial structural materials with diverse and extensive applications. Cermets are classified into various types based on their ceramic phases—carbide, oxide, carbonitride, boride-based, and those featuring graphite or diamond-like carbon [1-5]. Oxide-based metal ceramics, comprised of oxides such as alumina, zirconia, or their composites as the hard phase, and metals or alloys as the bonding phase, represent heterogeneous composite materials. This category of materials typically exhibits high hardness and good thermal stability, and finds significant applications in aerospace, automotive manufacturing, medical devices, electronic components, and other fields[6].Carbonitride-based cermets, developed on the foundation of carbide-based cermets, have emerged as a new class of cermet developed on the foundation of carbide-based cermet, exhibiting high hardness, strength, excellent high-temperature and wear resistance, good toughness, low density, and high thermal conductivity. Currently, this class of materials is undergoing robust development and has widespread applications in areas such as machining, high-temperature components in engines, and sealing

Received date:
Foundation item: National Natural Science Fund of China (52376076), Material Corrosion and protection Key Laboratory of Sichuan Province open fund(2023CL13), Laiwu Vocational and Technical College Teacher's Research Fund (2023jsky05)
Corresponding author: Huang Bensheng, Ph.D., Professor, School of New Energy and Materials, Southwest Petroleum University, Chengdu 610500, China, Tel: 13980965798，E-mail: hbslxp@163.com

elements in the petroleum industry [7-11]. Detailed exploration of boride-based cermet commenced relatively late, beginning in the 1980s. Research has indicated that metal borides possess high thermal conductivity and temperature stability, making them suitable for applications requiring excellent wear resistance, such as cutting tools, rock drilling tools, and wear-resistant components. However, owing to their low strength and high brittleness, these materials are unsuitable for use under impact loads [12-14]. Graphite-metal composite materials are employed in various electrical contacts and extensively used for manufacturing brake linings and clutch facings. Additionally, these materials can incorporate diamond-like carbon, ranging from coarse fragments to fine powders, within a metal matrix for the produce cermets used in grinding, polishing, sawing, cutting, dressing, and shaping tools [15-17]. Carbide-based cermets primarily consist of metals and carbides. These materials typically exhibit outstanding thermal, mechanical, and chemical stabilities, making them widely applicable in high-temperature, high-pressure, and corrosive environments. Among these, tungsten carbide and titanium carbide-based cermets have a long development history and find a broad range of applications [18].

The WC-Co cermet possesses the most favourable composition and optimal atomic interactions in terms of mechanical performance. The crystal structure of WC is cubic, with carbon atoms (C) forming covalent bonds with tungsten atoms (W), providing high hardness and excellent wear resistance. The role of Co is to consolidate and bond tungsten carbide particles, while also providing toughness and ductility. The crystal structure of Co is hexagonal and close-packed and remains stable at room temperature. The bonding between Co and WC is facilitated by the plastic deformation ability of Co, enabling it to fill the gaps between the WC particles and form strong connections. Both metal-metal bonds and some metal-nonmetal exist between Co and WC. Owing to the combination of covalent bonding in WC and metallic and nonmetallic bonding in Co, WC-Co alloys exhibit excellent mechanical properties such as hardness, toughness, and wear resistance. These intricate atomic interactions impart unique properties to WC-Co alloys, making them crucial materials for numerous industrial applications [19-24]. However, such alloys are becoming rare with the excessive exploitation of resources, in particular, tungsten reserves in China have sharply declined, and the advantage may be lost. Additionally, the critical element, Co, primarily coexists with minerals such as nickel, copper, manganese, and iron. Insufficient geological reserves, low-grade deposits, and production difficulties in Co resources in China have highlighted a need to develop cost-effective cermets without tungsten and Co, which have significant economic and strategic importance [25-27]. In addition, WC can undergo oxidation at high temperatures, which affects its performance. Preventative measures, such as special protective coatings or alloying are required when using WC in oxidising environments. Yan et al. found that adding WB to WC-Co can lead to the in-situ formation of WCoB. Thermal analysis demonstrated that the high-temperature oxidation resistance of WCoB surpassed those of WC and Co, suggesting that adding WB can significantly enhance the high-temperature oxidation resistance of WC-Co [28].

TiC has a higher melting point (3250 ℃) compared to that of WC (2870 ℃), exhibits excellent wear resistance, and its density, at 4.93 g/cm^3, is only approximately one-third of WC (15.63 g/cm^3) [29]. Moreover, TiC can be wetted by Co, because of its relatively low cost and abundant Ni content, making it a potential substitute for the widely used WC-Co-based cermet, resulting in considerable cost reductions. Compared with tungsten resources, titanium resources are more abundant in the Earth's crust, and their production costs are relatively low [30-32]. At elevated temperatures, TiC forms a stable titanium oxide film in an oxidising atmosphere, providing a certain level of protection and slowing down further oxidation of the material. Consequently, TiC often exhibits superior oxidation resistance in high-temperature applications [33]. TiC typically demonstrates good oxidation resistance at high temperatures, superior to that of WC.

TiC-NiCr cermets represent a novel class of materials characterised by high-temperature resistance, wear resistance, corrosion resistance, and a balanced combination of excellent toughness, strength, and thermal conductivity. Studies have demonstrated that incorporating other metals into the Ni bonding phase metal can enhance the high-temperature strength of the 7metal phase. NiCr, which serves as the bonding phase against the hard phase, not only exhibits good wettability and considerably improves toughness, high-temperature strength, oxidation resistance, and corrosion resistance [34-36].

Currently, there is limited research on the preparation and high-temperature performance of TiC-based metal-ceramics using NiCr as the sole bonding phase remains limited. This study addresses this gap by optimising the powder metallurgy process used in manufacturing metal−ceramics based on previous experience. TiC-NiCr metal−ceramics with uniform structures and excellent properties were successfully prepared, with their hardness and flexural strength reaching Rockwell hardness (HRC) values of 65 and 1450 MPa, respectively. In addition, this research focused on the high-temperature oxidation of TiC-based metal ceramics. While previous studies typically explored temperatures below 800 ℃ and durations under 100 hours [37-39], this investigation extends to 0−1000 hours at 900 ℃. Examining the long-term oxidation resistance of TiC-NiCr metal−ceramics at elevated temperatures provides valuable insights for material performance assessment, enhancement of oxidation resistance, industrial manufacturing, energy conservation, environmental protection, material selection and design, and research on protective materials.

2 Experiment

2.1 Raw materials and sample preparation

In this study, experiments were conducted using TiC, Ni and Cr powders as the raw materials. The average particle size of the raw materials is below 50 μm, with the oxygen content not exceeding 0.5%. The composition ratios are listed in Table 1.

The powder was uniformly mixed using a combination of dry mixing and wet grinding methods, as shown in Figure 1. For the dry mixing process, the pre-prepared powders, as specified in the composition table, were introduced into an automatic mixer and mixed for 2 h. The wet grinding process involved the using an XGP36X planetary ball mill, with the addition of high-speed steel balls and anhydrous ethanol during the wet grinding process, at a ball-to-material ratio of 3:1 and a liquid-to-solid ratio of 2:5.

Table 1 Chemical composition of materials（wt%）

Marks	TiC	Cr	Ni
Content	60	10	30
D50(μm)	11.81	38.59	11.58

After wet grinding for 24 hours, the slurry was discharged and sieved through a 380 μm screen. Subsequently, the material was dried in a vacuum oven at 65 ℃ for 8 hours, followed by sieving through a 250 μm screen. To facilitate subsequent compaction and moulding, a certain proportion of polymer binder was added, mixed thoroughly, and dried again. The resulting material was sieved through a 380 μm screen and kept for further use. Compaction and moulding were performed using a Y41-63 type 60-ton single-column hydraulic press, with the specimens were then subjected to vacuum sintering in a ZTS-40/40/80 integrated vacuum sintering and debinding furnace. The maximum sintering temperature was 1420 ℃, with a 40-minute insulation period. A TiC-NiCr cermet composite that met the specified requirements was obtained after testing. After sintering, the dimensions of the specimens were ø20×40 mm.

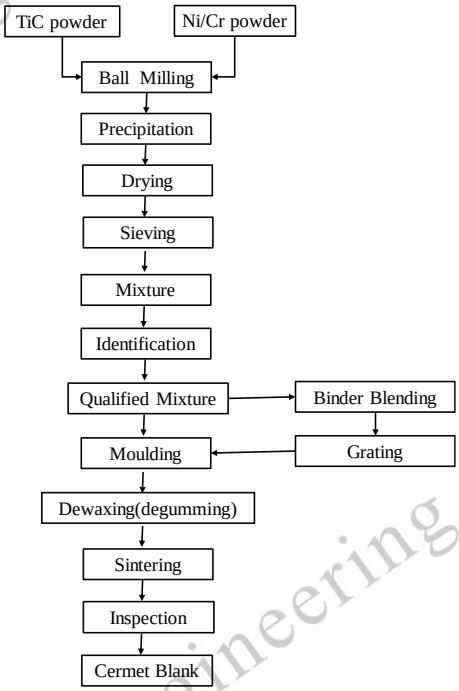

Fig.1 Process flow diagram

The sintering process of TiC-NiCr cermet is a thermal processing technique involving a series of physical and chemical transformations, transforming agglomerates of powder into aggregates of grains, ultimately yielding a product with the desired physicochemical properties. Consequently, the sintering process plays a crucial role in determining the performance of the final product. The sintering temperature profile of TiC-NiCr cermet in this experiment is depicted in the accompanying Figure 2.

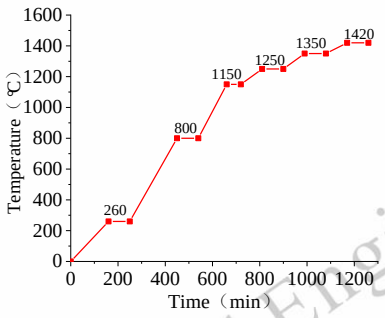

Fig.2 Curve of sintering process

2.2 Performance testing and microstructure analysis

2.2.1 Mechanical Property

After mechanical polishing of the specimens, the density was measured using an ES-J200D density balance, the hardness was determined using an HR-150A Rockwell hardness tester, and the flexural strength was assessed using a three-point bending test on a HAW-1000D universal testing machine. Typically, the processed specimens (with dimensions of 30 mm × 5 mm × 5 mm) were positioned on a universal

testing machine for three-point bending strength testing, with the test parameters set at a span of 20 mm and a loading rate of 0.05 mm/min. The principles of the three-point bending strength experiment are illustrated in Figure 3.

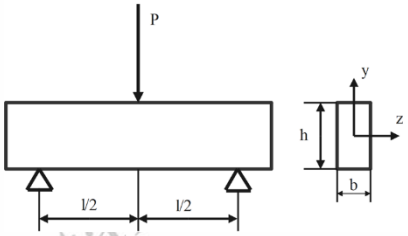

Fig.3 Schematic diagram of flexural strength experiment

Three-point bending strength calculation formula：

$$\sigma = \frac{3PL}{2bh^2} \qquad (1)$$

In the formula: σ represents the flexural strength (MPa), P is the maximum load (N), L is the span (mm), B is the specimen width (mm), and h is the specimen thickness (mm). The flexural strengths of the cermet specimens were determined using the three-point bending method, with five tested specimens, and the average value was calculated.

2.2.2 Oxidation mechanism experiment

The purpose of oxidation experiments is typically to investigate the oxidation mechanisms and reaction kinetics of materials under various conditions, such as temperature, pressure, and gas composition. The simplest method for such experiments involves placing a sample of known mass and surface area in an air atmosphere, heating it for a specific duration, removing the sample, allowing it to cool, and then weighing it to determine the extent of oxidation. The morphologies of the oxidised samples were observed and characterised using techniques such as X-ray diffraction (XRD) and scanning electron microscopy (SEM).

The oxidation reaction of metals is typically initiated by the formation of an oxide film on the metal surface. Therefore, the process of metal oxidation generally encompasses two stages: the formation stage of the oxide film and the growth stage of the oxide film. The formation stage of the oxide film primarily includes oxygen adsorption on the metal surface, nucleation of oxide species, lateral growth of oxide nuclei, and the development of a tightly adherent oxide film. After the formation of an exceedingly thin oxide film on the surface, as oxidation proceeds, the oxide film entered the growth stage as oxidation proceeded. Based on the aforementioned mechanism, the specimens were polished with #2000 grit sandpaper after cutting, followed by ultrasonic cleaning in anhydrous ethanol and subsequent drying. The specimens were then placed in pre-weighed Al_2O_3 crucibles and subjected to cyclic oxidation experiments in an OTF-1200X tubular resistance furnace. The temperature was set at 900 ℃, and the duration was 1000 h. The specimens were removed every 100 h and allowed to cool naturally to room temperature in ambient air. Their masses were measured using an electronic balance with an accuracy of 0.01 mg. The increase in the oxidation mass per unit area was calculated, and three specimens were tested for each alloy composition, with the average values obtained.

Surface phase analysis of the oxidised specimens was performed using a D8 ADVANCE X-ray diffractometer (Bruker). The surface and cross-sectional morphologies of the oxide films were observed using an EVO10 field-emission scanning electron microscope, with micro-area composition analysis was conducted using an attached energy-dispersive spectrometer.

3.Results and discussion

3.1 TiC-NiCr Microstructure

3.1.1 Microstructure

A typical structure of the TiC-NiCr Cermet after vacuum sintering is shown in Figure 4. The TiC ceramic phase exhibited an irregularly shaped, nearly spherical or square morphology, whereas the NiCr metal phase was uniformly distributed. The microscopic structure of the material revealed that small ceramic-phase particles were evenly dispersed within the continuous NiCr metal phase. The metal phase formed a continuous matrix that encapsulated the uniformly distributed ceramic particles. The particle size of the TiC ceramic phase is approximately 5−10 μm. Figure 5 shows the energy dispersive spectroscopy (EDS) elemental surface distribution map, clearly illustrating the distribution of TiC particles within the metal bonding phase. Ni and Cr distinctly surrounded the TiC particles, with Ni, in particular, exhibiting enrichment in a circular pattern around the TiC particles. The distribution of Cr is relatively scattered, and studies indicate that a portion of Cr forms a face-centred cubic structure Ni (Cr) solid solution, whereas another portion exists in elemental form.

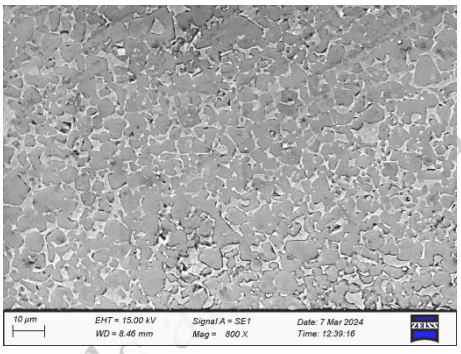

Fig.4 Microstructure of TiC-NiCr cermet

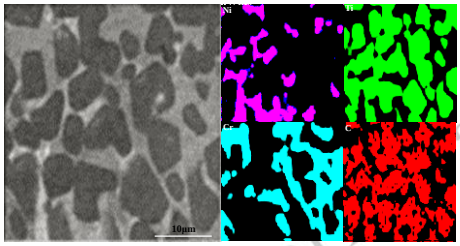

Fig.5 Element Mapping of TiC-NiCr cermet

3.1.2 Formation Mechanism of Microscopic Structure

Sintering of metal ceramics falls under the category of liquid-phase sintering. Liquid-phase sintering can be divided into three stages with indistinct boundaries: (1) the generation of the liquid phase and particle rearrangement;(2) the dissolution/precipitation of the solid phase (solid-phase diffusion, grain growth, and shape adjustment); and (3) the formation of a solid-phase framework (elimination of pores, grain growth, and contact enlargement). The evolution of microstructural changes and densification behaviour varied across these stages (as shown in Figure 6), and the proportions of each stage were influenced by factors such as particle size, particle shape, heating rate, density, and particle composition. In the context of TiC-NiCr cermet, the overall sintering process can be delineated into the following four stages: The first stage occurs below 800 ℃ and can be further subdivided into the pre-sintering stage (0−260 ℃) and the degreasing sintering stage (260−800 ℃), which involves the removal of the easily sintered and volatile binder from the green compact (as shown in Figure 6a). In this stage, the primary chemical transformations involved the gradual decomposition and carbonisation of the polymer binder within the compact under heating, with a slow expulsion through the interparticle pores. During this stage, changes occur in the state of the powder particles, initiating surface diffusion and enhancing the compaction strength. The sintering curve for this stage was set at a relatively low heating rate, primarily to prevent rapid carbonisation reactions and volatilisation of the binder, which could lead to the formation of internal voids and defects, thereby affecting the final density of the sintered product.

The second stage occurs between 800 ℃ and 1280 ℃ (the eutectic temperature) and represents the phase of liquid formation and particle rearrangement in the cermet powder (as depicted in Figure 6b). Within this temperature range, liquid-phase Ni gradually formed as the temperature increased, facilitating surface diffusion and volume diffusion between the TiC particles. The solid-phase particles of TiC and Cr exist in a suspended state within the Ni liquid phase, driven by the surface tension of the liquid phase, leading to a gradual reduction in the distance between the TiC particles and rapid densification. With the increasing temperature, the diffusion of Ni intensified, bringing the TiC particles closer together and resulting in substantial volume shrinkage of the sintered sample. Meanwhile, the solubility of Cr in Ni gradually increased, leading to the formation of an increasing amount of Ni-Cr solid solution.

The third stage occurs between 1280 ℃ (eutectic temperature) and 1380 ℃ (sintering temperature) and represents the solid-phase dissolution-precipitation stage (as shown in Figure 6c). Within this sintering temperature range, a significant amount of the liquid phase appeared. Simultaneously, the TiC grains formed a skeletal structure in the liquid phase of the Ni-Cr solid solution, initiating the contraction of the blank and forming the primary organizational framework. During this process, a thin layer of liquid phase is formed on the surface of the Ni-Cr, providing lubrication between the TiC particles and reducing the friction between them. Under the influence of liquid phase surface tension, TiC particles are prone to undergo rearrangement, further enhancing densification. During this sintering process, dissolution-precipitation phenomena also occur because of the high surface energy of the local TiC particles. Under these sintering temperature conditions, the TiC particles easily dissolved in the liquid phase and precipitated in other regions. Consequently, this led to the preferential growth of TiC grains along a specific direction. This growth pattern promoted bonding or aggregation among adjacent TiC grains, causing a gradual transformation of the grain morphology into a spherical shape. Simultaneously, smaller grains diminished or disappeared, whereas larger grains enlarged further. Consequently, a TiC skeletal structure was formed within the sintered sample.

The fourth stage occurs at 1380−1450℃ (sintering temperature), i.e.,the sintering stage (as shown in Figure 6d). After the three stages, the TiC particles approached, contacted and combined to form a continuous skeleton. The remaining Ni-Cr liquid phase filled the voids in the skeleton. At this stage, the existence of a solid skeleton prevents the further rearrangement of the particles because of its rigidity, resulting in a significant decrease in the densification rate.

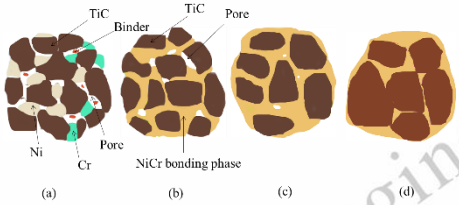

Fig.6 Schematic of the densification behavior and microstructure evolutionfor the three overlapping stages in cermet [40].

3.2 Oxidation resistance of TiC-NiCr

3.2.1 Oxidation Kinetic Curves

Figure 7 reveals that during the 1000h high-temperature oxidation at 900 ℃, the TiC-NiCr metal ceramic exhibits a linear fluctuating growth trend in the initial oxidation period (<500h). The oxidation weight gain rate accelerates at the onset of oxidation, attributed to the dynamic changes in the formation and disruption of the oxide-layer protective film. In this initial phase,

the oxide layer is extremely thin, and because of the short diffusion paths, the atoms participating in the reaction within the matrix easily reach the oxidation reaction interface through the oxide layer, resulting in a faster oxidation rate. With a prolonged oxidation time (>500 h), the weight gain rate significantly decreased. The oxide layer thickened and underwent lateral growth, and the diffusion rate of the ions involved in the reaction decreased. Consequently, the weight gain due to oxidation decreased, and the oxidation rate slowed, showing an overall linear growth trend, indicating that as the surface oxide layer gradually thickens, it becomes more stable and denser, reducing the surface porosity and impeding further oxidation. Metal−ceramics exhibit improved oxidation resistance.

To derive the oxidation equation, the experimental data in Table 2 were processed using the formula $W^n=Kt$ as the fitting equation. The oxidation kinetics equation was then fitted using the least squares method [41], following the steps outlined below:

$$n\lg W=\lg K+\lg t \quad (2)$$
$$\lg t=n\lg W-\lg K \quad (3)$$

Substituting the data from the table into Equation (2) and performing the calculations, we obtained: n=5.2531and K=1131.4.

Therefore, the oxidation kinetics equation is： $W^{5.2531}=1131.4t$，The curve of the oxidation kinetics equation is shown alongside the curve of weight gain due to oxidation in Figure 7.

Table 2 Oxidative weight gain data

t(h)	300	400	500	600	700	800	900	1000
W(g/m^2)	388	434	560	581	588	593	617	636

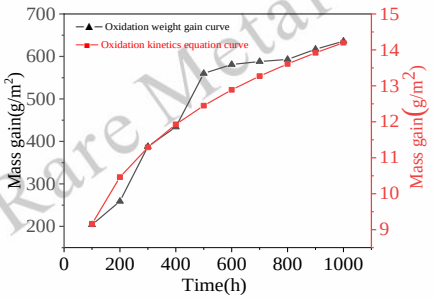

Fig.7 Oxidation kinetics equation curve and Oxidation weight gain curve of the TiC−NiCr cermet at 900℃

By comparing the weight gain due to oxidation and the oxidation kinetics equation of TiC-NiCr cermet at 900 ℃, it is observed that the actual degree of oxidation is significantly higher than the theoretical calculation, and the process is more rapid and intense. The oxidation of metal ceramics is influenced not only by its own composition but also by two main factors: density and the protective oxide layer. Density has a significant impact on the oxidation resistance of a material. Oxygen easily permeates through the pores or defects in non-dense materials, thereby accelerating the oxidation reaction rate. The magnitude of the porosity has a noticeable effect on the activation energy of the oxidation process. As the porosity increases, the activation energy decreases, leading to a reduction in the oxidation resistance. The protective oxide layer, formed by a dense oxidation layer, hinders the penetration of oxygen, and reduces or prevents material loss. Therefore, enhancing oxidation resistance is important.

3.2.2 Performance changes before and after oxidation

After exposure to high-temperature oxidation at 900 ℃, a distinct oxide layer was formed on the surface, which considerably reduced the surface hardness of the TiC-NiCr metal−ceramic from 65.5 HRC to 38 HRC. After removing the surface oxide layer, the hardness of the samples was measured after 200, 400, and 800 h at 62, 61, and 60.5 HRC, respectively. The hardness showed a slight decrease with no significant variation, indicating that the oxide layer played a protective role. Considering the potential errors in the oxidation tests and hardness measurements, the oxidation test did not affect the hardness of the TiC-NiCr cermet matrix. Figure 8 illustrates the variation in the flexural strength with different oxidation times. The flexural strength of the unoxidised sample was within 1300−1500 MPa. After 1000 h of oxidation, the minimum flexural strength was 790 MPa, indicating the effect of the oxidation process on the flexural strength of the material, which gradually decreased with prolonged oxidation time. The flexural strength of cermets is closely related to the internal sources of fractures, such as pores. In Figure 8, a significant inflection point is observed at 300 h, indicating that in the early stages of oxidation, the oxidation not only occurs on the surface of the metal−ceramics and penetrates the material's interior through defects such as pores, leading to an increase in fracture sources and a rapid decrease in flexural strength. After 300 h, a stable and moderately thick oxide layer form on the surface, impeding the enlargement or addition of fracture sources and thereby slowing down the decline in flexural strength.

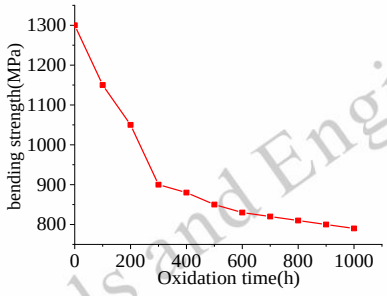

Fig.8 Flexural strength variation of the TiC-NiCr cermet at 900℃ for 1000h

3.2.3 Microscopic characteristics of oxide layer

3.2.3.1 Surface morphology and composition analysis of oxide layer

After prolonged oxidation at 900 ℃, TiC-NiCr cermets de-

velop a dense brownish oxide layer on the surface, exhibiting a metallic lustre. As the oxidation time increased, the colour of the oxide layer deepened, and the layer remained firmly adhered to the surface, demonstrating good integrity. No instances of oxide layer detachment were observed for any of the samples. The morphology of the surface oxide layer is shown in Figure 9. Figure 9 illustrates that the TiC-NiCr cermet generated a substantial amount of irregularly shaped, granular oxides on the surface after oxidation at 900 ℃ (Figures 9a, c, e). Additionally, with increasing oxidation time, the particles size gradually accumulated and enlarged, forming columnar or elongated Rutile Titanium Dioxide, with the connections between particles becoming progressively tighter (Figures 9b, d, f). XRD analysis of the oxidised surface (Figure 10) revealed the presence of predominantly TiO_2 with trace amounts of $NiTiO_3$. With increasing oxidation time, TiO_2 exhibited enhanced stability, gradually forming a dense oxide layer. The presence of rapidly increasing TiO_2 content inhibited the reaction peak of $NiTiO_3$, leading to its attenuation.

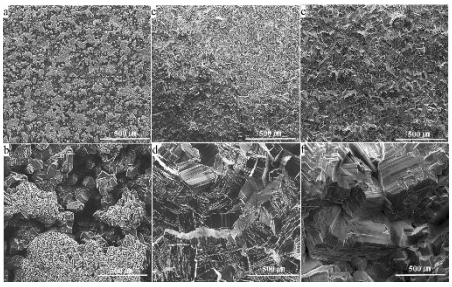

Fig.9 TiC-NiCr cermet microstructure at 900℃ for the different sintering times:(a,b) 200h, (c,d) 500 h, and (e,f) 800 h

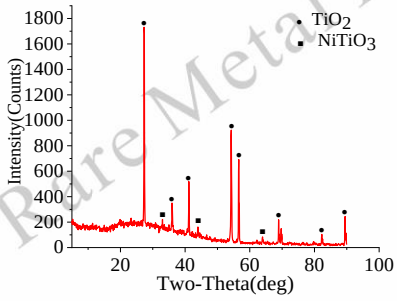

Fig.10 XRD patterns of the TiC-NiCr cermet oxide layer at 900℃

3.2.3.2 Morphology and composition analysis of oxidation cross section

Figure 11 shows the cross-sectional morphology of the oxide layer. With increasing oxidation time, the thickness of the oxide layer noticeably increases, expanding from approximately 80 μm to around 260 μm, with the maximum oxidised impact zone reaching 300 μm. A distinct dark oxide layer can be observed, featuring a dark color and a matrix structure containing granular titanium carbide were observed. The oxide layer was clearly divided into two layers: an outer layer with a loose structure and abundant pores that exhibited higher Ti and O contents. Combined with the XRD analysis, the predominant oxide in the outer layer was TiO_2, with a minor amount of $NiTiO_3$. In contrast, the inner oxide layer was relatively dense. The formation of this dense oxide layer was responsible for the decrease in oxidation rate over time.

A comparative analysis reveals that in Figure 11(a), with an oxidation time of 100 h, the loose structure of the oxide layer is relatively inconspicuous, with smaller and less widespread pores. As shown in Fig 11(b), after 500 h of oxidation, the loose structure became more pronounced, exhibiting numerous and widely distributed pores. Figure 11(c) shown that after 800 h of oxidation, the loose structure and pore size decreased. Additionally, the bottom of the inner oxide layer exhibited a branched, intermittent distribution of the inner oxide layer, penetrating into the surface layer of the matrix.

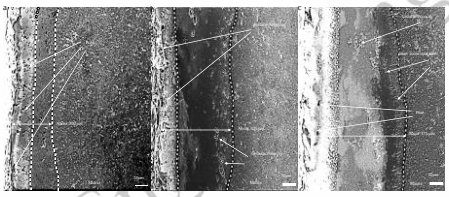

Fig.11 Cross-sectional microstructure of the oxide films of TiC-NiCr cermet oxidized at 900℃for different oxidation times:(a)200h, (b)500h, and(c)800h

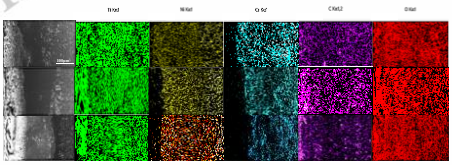

Fig.12 Element mapping of oxide films of TiC-NiCr cermet at 900℃for different oxidation times: (a) 200h, (b)500h, and(c)800h

A distinct layered structure of the oxide layer was observed through the analysis of the distribution of different elements, as shown in Figure 12. The surface oxide layer was primarily composed of Ti and O, and XRD analysis (Figure 13) indicated that the upper oxide layer was predominantly TiO_2, with a minor presence of unoxidised TiC. The inner layer exhibited higher concentrations of Ni and Cr, forming a dense structure with a whitish appearance. In addition, Ni, Cr, and C are enriched at the interfaces between the upper and lower oxide layers. The XRD analysis (Figure 13) revealed that the main components of the oxide layer were TiO_2, NiO, Cr_2O_3, and small amounts of Ni-TiO_3 and $NiCr_2O_4$.

$$TiC(s)+3/2O_2(g)\rightarrow TiO_5(s)+CO(g)(4)\Delta G^{\ominus}{}_{R900}=-1132.46KJ/mol$$
$$Ni(s)+1/2O_2(g)\rightarrow NiO(s)(5)\Delta G^{\ominus}{}_{R900}=-180.04KJ/mol$$
$$Cr(s)+3/4O_2(g)\rightarrow 1/2Cr_2O_3(s)(6)\Delta G^{\ominus}{}_{R900}=-955.07KJ/mol$$
$$NiO(s)+TiO(s)\rightarrow NiTiO_3(s)(7)\Delta G^{\ominus}{}_{R900}=-20.74KJ/mol$$
$$NiO(s)+Cr_2O_3(s)\rightarrow NiCr_2O_4(s)(8)\Delta G^{\ominus}{}_{R900}=-48.33KJ/mol$$

The reactions (4) and (5) reveal that, during the oxidation process, TiC generates a certain amount of gas, contributing to the formation of pores and looseness. Thermodynamic analy-

sis indicated that TiC exhibited the highest propensity to react with oxygen, followed by Cr, whereas Ni demonstrated the weakest oxidation reaction capability. By investigating the oxidation products of the alloy in air at 900 ℃, the primary oxides underwent further solid-state reactions (7) and (8), leading to the formation of $NiTiO_3$ and trace amounts of $NiCr_2O_4$.

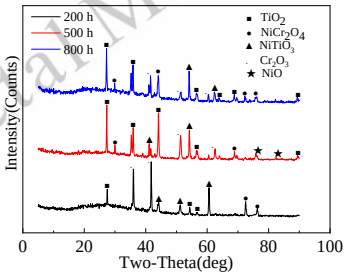

Fig.13 XRD patterns of oxidized surface of TiC-NiCr cermet oxidized at 900℃ for 200 h ,500h and 800 h in static air

3.2.3.3 Microstructure and compositional analysis of oxidation products

After 1100 h of prolonged oxidation, the ongoing reactions led to the development of cracks and defects in the oxide layer, serving as pathways for the oxidation reaction to progress to deeper layers. Solid-state reactions (4) and (5) penetrated deeper, subsequently triggering the continuous advancement of reactions (1), (2), and (3). Consequently, the entire oxidation process gradually intensified, ultimately resulting in the complete oxidation of the sample. Therefore, NiO is further consumed during the process. As shown in Figure 14, the oxide layer is distinctly divided into white (a (1)) and a light-grey regions (b (2)). SEM and EDS analyses of the light-gray region in Figure 15 reveal that this region is primarily composed of TiO_2, attributed to the considerably higher TiC content compared to that of Ni, resulting in TiO_2 being the predominant final oxidation product. Analysis of the white region in Figure 16 shows compositional elements such as O, Ti, and Ni, confirming the white region is $NiTiO_3$. Notably, owing to the lightweight nature of O atoms in EDS detection, a relatively large deviation might be observed in atomic ratios in the detected results compared with the anticipated atomic compositions of TiO_2 and $NiTiO_3$ [42].

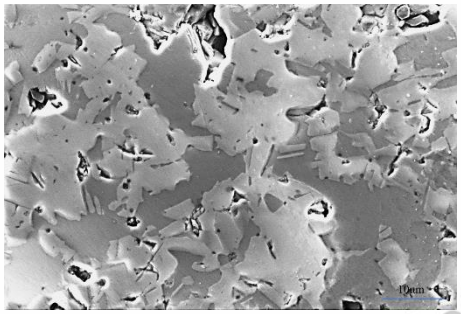

Fig.14 Microstructure of the TiC-NiCr cermet oxide layer at 900℃ for 1100h

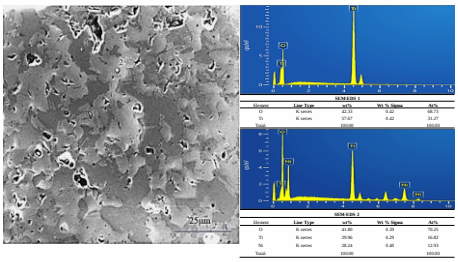

Fig.15 SEM image of chemical composition analysis results. (a) SEM-SE image of the composite. (b) EDS map-scanning results in (1,2).

The content of Cr_2O_3 is relatively low, and elemental distribution maps across the cross-section of the oxide layer, as well as XRD analysis, revealed its predominant presence at the bottom of the oxide layer. Cr_2O_3 exhibits a linear distribution, gradually forming a relatively continuous and completely layered structure with increasing oxidation time. The analysis of typical oxidation products also indicated a high correlation between the distributions of Cr and O elements, confirming the presence of Cr_2O_3.Simultaneously, a small amount of Cr was elements is observed at different positions in the elemental distribution map (Figure 19). Cr_2O_3 primarily nucleates at the grain boundaries on the alloy surface, whereas NiO nucleates across the entire surface. Owing to its rapid growth rate, NiO formed a continuous NiO oxide layer covering the Cr_2O_3 nuclei, resulting in the formation of an external NiO oxide layer (containing Cr_2O_3 particles). As oxidation progressed, Cr_2O_3 gradually formed, and the oxygen partial pressure at the interface of the oxide film/matrix interface rapidly decreased. When the oxygen partial pressure fell below the equilibrium decomposition pressure of NiO, NiO growth ceased. Under severe oxidation conditions at 900 ℃ for 1100 h, the internal oxidation of Cr occurs because of its low content. Cr_2O_3 particles are formed within the matrix, and as the external oxide layer advances into the matrix, most of the internally oxidised Cr_2O_3 particles are engulfed by NiO. The result of the solid-state reaction is the generation of $NiCr_2O_4$, which forms an outer layer of NiO, an intermediate layer of spinel-type $NiCr_2O_4$, and a very thin inner layer of Cr_2O_3 with a minor occurrence of internal oxidation of Cr.

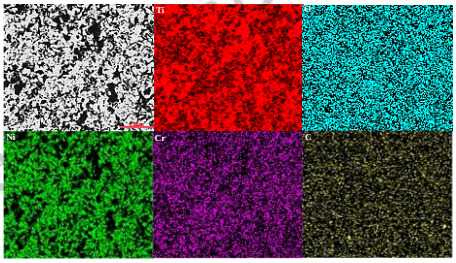

Fig.16 Element mapping of the oxidation microregion

4 Discussion

4.1 Sintering Analysis of TiC-NiCr Cermet

The porosity, theoretical density, relative density, and shrinkage of the TiC-NiCr cermet prepared via powder metallurgy are presented in Table 3. The notation A04B00 indicates that the volume fraction of A-type pores with sizes smaller than 10 μm is 0.06%, with no B-type pores in the 10−25 μm range, indicating that the sample exhibited good density after sintering, with low porosity—a characteristic attributed to its liquid-phase sintering properties. Densification of the metal−ceramic relies primarily on the plastic flow of the NiCr metallic phase and the rearrangement of the TiC-ceramic phase particles, accompanied by the simultaneous elimination of voids within the material. The driving forces for densification primarily stem from two aspects: the surface tension of the liquid phase acting on the pores and the capillary forces generated by the liquid phase penetrating solid-phase particles. Liquid-phase sintering con-sists of three stages: flow, dissolution, and precipitation of the liquid phase, and sintering of the solid phase. During the liq-uid-phase plastic flow, the particles rearranged into the most closely packed configuration, rapidly increasing the density of the sintered body. In the rearrangement stage, although pore elimination and particle rearrangement occur swiftly, leading to a rapid densification process, the formation of bridges between particles, after they converge to a certain extent, introduces in-creased resistance to the viscous flow of the liquid phase. Consequently, the green compact could not achieve complete density. Full densification requires the completion of two stages. In the second stage, as the gas pores are essentially eliminated and the particle spacing decreases, infiltration of the liquid phase into the remaining pores becomes more challenging. Hence, compared to the preceding stage, the densification rate slows. In the third stage, the solid-phase skeleton introduced rigidity, hindering further particle rearrangement and leading to a significant reduction in the densification rate. The toughness of liquid-phase sintering densification in metal–ceramics de-pends on three fundamental conditions related to the properties of the liquid phase:1) wetting of the NiCr liquid phase on the surface of the TiC particles, 2) solubility of the TiC particles in the liquid phase of the NiCr matrix, and 3) quantity of the liq-uid phase at the sintering temperature. Wetting is determined by the surface tensions γ_L and γ_S of the liquid and solid phases, as well as the interfacial tension γ_{SL} between the two phases. When the NiCr liquid phase wets the TiC particles, the equilibrium thermodynamic condition at the contact point is given by $\gamma_S = \gamma_{SL} + \gamma_{L\cos\theta}$, where θ represents the wetting angle of the liquid phase with respect to the solid phase. As the temperature rises, θ gradually decreases [43].

Table 3 Porosity, theoretical density, relative density, and shrinkage of TiC-NiCr cermet

Marks	porosity	Theoretical density(g/cm^3)	relative density	shrinkage ratio(%)
TiC-NiCr cermet	A04B00	6.2	0.98	0.87

4.2 Oxidation-protective property of the coating

Previous studies have indicated that the high-temperature oxidation behaviour of the experimental materials is influenced by both kinetic and thermodynamic factors [44]. According to the relevant data in the "Handbook of Inorganic Thermodynamics", the calculation formula for the Gibbs free energy function of the substance under constant pressure conditions during oxidation of the studied alloy is as follows:

$$\left|\Delta G^{\Theta}_{TiC}\right| > \left|\Delta G^{\Theta}_{Cr}\right| > \left|\Delta G^{\Theta}_{Ni}\right| > \left|\Delta G^{\Theta}_{Cr_2O_3}\right| > \left|\Delta G^{\Theta}_{TiO_2}\right|$$

According to the second law of thermodynamics, the change in the Gibbs free energy serves as a criterion for assessing the spontaneity of a reaction. When $\Delta G = 0$, neither forward nor reverse reactions proceed spontaneously. In the case of $\Delta G > 0$, the reverse reaction occurs spontaneously, while for $\Delta G < 0$, the forward reaction takes place spontaneously. For the oxidation reactions mentioned above, the Gibbs free energy changes remain negative at an oxidation temperature of 900 ℃, indicating that these reactions proceeded spontaneously from left to right. A lower Gibbs free energy value (negative) signifies a higher priority for the formation of the corresponding oxide. The order of the respective Gibbs free energies for the aforementioned reactions was calculated as follows:

$$\triangle G^{\theta}_{T} = \triangle H^{\theta}_{T} - 298 \triangle S^{\theta}_{T}$$

The findings revealed that during the oxidation process, TiC exhibited the highest susceptibility to oxidation, followed by Cr and Ni. Subsequently, as the oxidation time progressed after the formation of the respective oxides, internal oxidation compounds such as $NiCr_2O_4$ and $NiTiO_3$ were generated. However, because of its significantly lower Cr content compared to that of Ni, although $NiCr_2O_4$ is relatively facile to form, its content remains limited and is primarily distributed in the inner oxidation layer. In summary, the structure of the oxide film on the surface was determined by both thermodynamic and kinetic factors. Under experimental conditions with elevated oxygen partial pressure, the surface underwent simultaneous oxidation during the initial stages of oxidation based on the composition of its elements. Specifically, TiO_2, NiO, and Cr_2O_3 nucleate simultaneously, with TiO_2 rapidly nucleating across the entire surface, forming a continuous TiO_2 oxide layer that covers/encapsulates the cores of NiO and Cr_2O_3. This layer impedes the outward diffusion of oxygen elements and the outward diffusion of Cr and Ni matrices. As oxidation progressed, the thickness of the oxide film continued to increase, and spinel-type oxides continued to form. The oxygen partial pressure at the interface

between the oxide film and matrix rapidly decreased, leading to the gradual cessation of the oxidation process.

5 Conclusions

1) In preparing TiC-NiCr cermets via powder metallurgy, a uniform and densely packed ceramic material with excellent properties was achieved by strictly controlling the raw material quality and optimising the process rationally. The sintering process of TiC-NiCr cermet involved liquid-phase sintering, ultimately resulting in a dense structure with TiC particles uniformly distributed within the NiCr matrix.

2) After high-temperature oxidation at 900 ℃, a dense oxide film was formed on the surface of TiC-NiCr cermet surface, outward expansion of oxidation reactions. Although no significant change was observed in the hardness of the inner layer, the overall flexural strength decreased. The TiC-NiCr cermet exhibited passivation during oxidation, and the dense oxide layer formed contributed to the improved high-temperature oxidation resistance. However, the oxidation products are unstable, with continuous oxidation of Ni and Cr possible. Therefore, pro-longed oxidation over approximately 1000 h can lead to sub-stantial material deterioration.

3) The oxidation weight gain of TiC-NiCr cermet at 900 ℃ fol-lows an approximately parabolic kinetic pattern over time, with the trends in the oxidation weight gain curve closely resem-bling those of the oxidation kinetic equation curve. Up to 500 h, the oxidation weight gain rate was relatively rapid before gradually stabilising, suggesting that the initial growth of the oxide layer hindered further oxidation. The oxidation process is characterised by passivation, and the formation of an oxide layer contributes to the enhanced oxidation resistance.

4) Under prolonged oxidation at 900 ℃, TiC-NiCr Cermet form an outer layer primarily composed of relatively porous TiO_2/NiO, with small amounts of Cr_2O_3. The inner layer consisted of a continuous and dense composite oxide film, including TiO_2/$NiTiO_3$/$NiCr_2O_4$/Cr_2O_3. This composite oxide film impedes the outward diffusion of Ni and Cr from the matrix, reducing the oxidation rate and ultimately hindering oxidation penetration into the material.

5) The high-temperature oxidation behaviour of the TiC-NiCr cermet was influenced by both kinetic and thermodynamic factors. TiC was the most prone to oxidation, followed by Cr and Ni. With the extension of the oxidation time after the formation of the respective oxides, internal oxidation compounds, such as $NiCr_2O_4$ and $NiTiO_3$, were generated. However, owing to the significantly lower content of Cr compared to that of Ni in the composition, although $NiCr_2O_4$ formed relatively easily, its content remains limited and is primarily distributed in the inner oxidation layer.

References

1 Zhou Yu. Ceramic Materials Science [M]. Beijing: Science Press, 2004: 3-135.

2 Ettmayer P.Lengauer W. The story of cermets[J].Powder Met.Inter.1989,21(2): 37-38

3 J. R. Dingerpov W. B. Crandall. Shi Jin. Cermet [M]. Shanghai: Shanghai Science and Technology Press, 1964: 2-20.

4 Jiang Yuhe. Chemistry of Nonmetallic Materials [M]. Beijing: Science and Technology Literature Press, 1992: 2-35.

5 Xu Qiang, Zhang Xinghong, Qu Wei, Han Jiecai. Research progress of cermets[J]. Cemented carbide, 2002, 19 (4): 221-225.

6 Yan Kangping. Engineering Materials [M]. Beijing: Chemical Industry Press, 2001.264-268

7 Mu Baichun.Strengthening and Toughening of Ceramic Materials[M].Beijing:MetallurgicalIndustryPress,2002.16-33,112-132,146-148.

8 Liu Ning et al. Ti (C, N) -based cermets [M]. Hefei University of Technology Press. September 2009.

9 He Congxun, Xia Zhihua, etc. Studies on Ti (C, N) -based cermets [J]. Rare metals and compounds. 1999 (1): 77-82

10 Hu, Zhang et al. Research progress of Ti (C, N) materials [J]. Materials: 2010,24 (23): 29-33

11 Liu, Feng et al. Research progress of Ti (C, N) -based cermets [J]. Jiangsu Ceramics, 2005, 38 (6): 20-23

12 Xiao Shuiqing, Wu Shanghua. Research progress on microstructure and properties of Ti (C, N) -based cermet materials [J]. Cemented carbide, 2014,31 (2): 112-119

13 Wu H, Zheng Y, Zhang J, et al. Preparation of Mo_2FeB_2-based cermets with a core/rim structure by multi-step sintering approach[J]. Ceramics International, 2019, 45(17): 22371-22375.

14 Yu HZ, Liu WJ, Feng P, et al. Synthesis and microstructure evolution during vacuum sintering of Mo_2FeB_2 based cermets[J]. International Journal of Refractory Metals and Hard Materials, 2014, 45: 48-52.

15 Ren X, Yu L, Liu Y, et al. Effects of extra boron addition on the liquid-state sintering process and properties of hard Mo_2FeB_2-based cermets[J]. International Journal of Refractory Metals and Hard Materials, 2016, 61: 207-214.

16 Wang Qinsheng. Superhard Materials and Products [M]. Zhengzhou University Press, 2006.

17 Zhao Min. Review of stone processing equipment and technology in China in recent ten years [J]. Stone, 2016 (2): 25-29.

18 Mancisidor A, Lunobilbao C, Vielma N J, Sanchez J M, Iturriza I. Effect of sintering atmosphere on densification, mechanical properties and diamond stability of prealloyed diamond impregnated composites obtained by free sintering[J]. Powder Metallurgy, 2014, (5): 362.

19 Atefeh Aramian, Seyed Mohammad Javad Razavi, Zohreh Sadeghi- an, et al. A review of additive manufacturing of cermets[J]. Additive Manufacturing, 2020, 33: 1-17.

20 Zhang Fenglin, Wang Chengyong, Song Yuexian. Strengthening and toughening of WC-Co cemented carbide[J]. Powder Metallurgy Technology, 2003, 21 (4): 236-240.

21 Wang Guodong. Cemented carbide principle[M]. Beijing : Metallurgical Industry Press, 1988 : 13-14

22 Liu Yong, Yang Jiangao. Gradient and new structure cemented carbide[M]. Changsha: Central South University Press, 2010: 22-35.

23 Li D, Liu Y, Ye J, Chen X F, Wang L. The enhancement of the microstructure and mechanical performances of ultrafine WC-Co cemented carbides by optimizing Cr_2(C, N) addition and WC particle sizes[J]. International Journal of Refractory Metals and Hard Materials, 2021, 97(1):105518.

24 Lu Z Y, Du J, Sun Y J, Sun G S, Zhang C Y, Kong X M. Effect of ultrafine WC contents on the microstructures, mechanical properties and wear resistances of regenerated coarse-grained WC-10Co cemented carbides[J]. International Journal of Refractory Metals and Hard Materials, 2021, 97:105516.

25 Gao Y, Yan M Y, Luo B H, Sheng O Y, Chen W, Bai Z H, Jing H B, Zhang W W. Effects of NbC additions on the microstructure and properties of non-uniform structure WC-Co cemented carbides[J]. Materials Science and Engineering A, 2017, 687:259- 268.

26 Pastor H. Present status and development of tool materials:Part I-cutting tools [J].Int. Journal of Refractory Metals and Hard Materials, 1987, 6(4):196-209.

27 Hisashi Suzuki, Koji Hayashi, Hideaki Matsubara. The Development and Present Status of Titanium Carbides Base Cermets [J]. Journal of Japan Metal Society, 1983, 22 (4): 312-319.

28 Xifeng Yan,Haibin Wang,et al. High-temperature oxidation and wear resistance of WC-Co based coatings with WB addition[J].Journal of the European Ceramic Society, 2019,39(10): 3023-3034.

29 Hayness WM. CRC handbook of chemistry and physics: 95th edition 2014-2015[M]. London: CRC Press, 2016.

30 NM.Parikh ,M.Humenik JR. Cermets:II, Wettability and microstructure studies in liquid phase sintering[J].Journal of the American Ceramic Society, 1957,40(9):315-320.

31 Foreign Cemented Carbide ' writing group. Cemented Carbides [M]. Beijing: Metallurgical Industry Press, 1976, p168-519.

32 Wang Panxin. Powder metallurgy[M]. Beijing: Metallurgical Industry Press, 1997.

33 Wang Shisen. Special Ceramics[M]. Changsha: Central South University Press, 2005.

34 Dalai R P, Das S, Das K. Development of TiC reinforced austenitic manganese steel[J]. Canadian Metallurgical Quarterly, 2014, 53(3):317-325

35 Wang Quanzhao, Liu Yue, Guan Dehui, et al. Effects of TiN content on microstructure and mechanical properties of Ti(C,N)-NiCr cermets[J].Journal of Metals, 2005,(11): 1121-1126.

36 Sun Wenli. Study on the preparation, microstructure and properties of Ti(C, N)-NiCr-based ceramics[D]. Wuhan: Huazhong University of Science and Technology, 2012.

37 MA Hui, Luo Ji. Preparation and high temperature oxidation properties of TiC-NiCrCoMo steel bonded cemented carbides [J]. Powder metallurgy technology, 2021, (39) 2: 147-152.

38 Yao Zhenhua. High temperature oxidation behavior of Ti (C, N)-based cermets[D]. Wuhan: Huazhong University of Science and Technology, 2007.

39 Feng Fan, Fan Jinglian, Cheng Huichao, Tian Jiamin. High temperature oxidation behavior and mechanism of Mo-TiC cermets [J]. Powder metallurgy materials science and engineering, 2012, (17)4 : 408-413.

40 Dai Wenjie, Pan Shiyan, Shen Xiaoping. Research progress of numerical simulation of liquid phase sintering process at mesoscopic scale [J]. Materials, 2019, (33) 9: 2929-2938.

41 Yao Zhenhua. High temperature oxidation behavior of Ti (C, N)-based cermets[D]. Wuhan: Huazhong University of Science and Technology, 2007.

42 Li Lingqun, Fan Jinglian, Tian Jiamin, Cheng Huichao , Zhang Hongbo. Modification of the interface and its influence on the performance of W-6 wt% TiC composite[J]. Materials Science & Engineering A, 819 (2021) 141442:2-9.

43 Dai J,Zhu J,Chen J,et al.High temperature oxidation behavior and research status of modifications on improving high temperature oxidation resistance of titanium alloys and titanium aluminides: A review[J].Journal of Alloys and Compounds,2010,685(3)784-798.

44 B. Meredith & D. R. Milner. The Liquid–Phase Sintering of Titanium Carbide[J]. Powder Metallurgy.2016(9):162-170.

TiC-NiCr 金属陶瓷的制备与高温氧化性能研究

张雷[1, 2, 4],黄本生[1,*]，解传娣[2, 4],陈根[5]，杜皎[2, 4]，孙海身[2, 3, 4]

(1. 西南石油大学新能源与材料学院， 四川 成都 610500)

(2. 山东省粉末冶金先进制造重点实验室, 山东 济南 271100)

(3. 北京科技大学，北京 100083)

(4. 莱芜职业技术学院, 山东 济南 271100)

(5. 昆山安意源管道科技有限公司, 江苏 昆山 215300)

摘 要：金属陶瓷以其优异的硬度、强度和耐磨性而闻名，广泛应用于航空航天、电子和采矿行业。目前，一个重要的研究挑战是通过改进陶瓷相和改变金属的类型和成分来提高金属陶瓷的机械性能和抗氧化性，同时降低生产成本。本研究采用粉末冶金法制备 TiC-NiCr，并对其在 900℃下的氧化行为进行了研究。结果表明，TiC-NiCr 结构均匀，具有优异的力学性能，硬度为 HRC65，抗弯强度为 1450 MPa。利用 x 射线衍射(XRD)和扫描电子显微镜(SEM)研究了 TiC 基陶瓷的高温氧化机理。Ni 和 Cr 元素的加入及其固溶体不仅结合了硬相 TiC，保证了陶瓷的物理性能，而且通过形成致密的复合氧化层，阻碍了氧化过程中的内部扩散，从而增强了陶瓷的抗氧化性。TiC-NiCr 金属陶瓷在 900℃下呈现出致密的氧化保护膜，可连续氧化约 1000 小时。本文提出了一种制备 TiC-NiCr 金属基复合材料的方法，并对其抗氧化性能进行了评价，为在降低生产成本的同时提高其力学性能和抗氧化性能提供了理论和实践依据。

关键词：TiC-NiCr；微观组织；高温氧化；热力学与动力学

作者简介：张雷，男，1984 年生，博士，西南石油大学新能源与材料学院， 四川 成都 610500，电话：15006341829，E-mail: zhanglei200303@163.com

通信作者：黄本生，男，1969 年生，博士，教授，西南石油大学新能源与材料学院， 四川 成都 610500 电话：13980965798，E-mail: hbslxp@163.com